Evaluation of optical arrangements for ballistic imaging in sprays

Evaluation of optical arrangements for ballistic imaging in sprays

Mattias Rahm,[1,*] **Megan Paciaroni,**[2] **Zhenkan Wang,**[3] **David Sedarsky,**[1] **and Mark Linne**[1,4]

[1]*Division of Combustion, Department of Applied Mechanics, Chalmers University of Technology, Gothenburg, Sweden*
[2]*Department of Physics & Engineering, Fort Lewis College, Durango, Colorado, 81301, USA*
[3]*Combustion Physics, Lund University, Lund, Sweden*
[4]*School of Engineering, University of Edinburgh, Edinburgh, UK*

[*]*mattias.rahm@chalmers.se*

Abstract: This work investigates the imaging performance, in terms of contrast and resolution, of two different time-gated ballistic imaging setups commonly used in spray research. It is shown that the two setups generate similar spatial resolution in the presence of scattering media. The simpler ($2f$) setup, however, is less sensitive to component misalignments and time-gate induced aberrations than the commonly used ($4f$) system. Measurements comparing both arrangements indicated slightly higher contrast for the $2f$ system under the densest conditions for small scatterers. Subsequent computational modeling confirmed the observed tolerance of the $2f$ system to misalignment and gate effects. The best performing setup was also compared experimentally to its non-time-gated shadow-imaging equivalent, to establish when the time-gate enhances imaging performance. It is shown that the time-gated setup generates higher contrast under almost all of the scattering conditions tested, while the non-time-gated setup generates higher spatial resolution only in the lower scatterer size range at the lowest scatterer concentrations.

OCIS codes: (110.0113) Imaging through turbid media; (190.3270) Kerr effect.

References and links

1. T. Fansler and S. Parrish, "Spray measurement technology: a review," Meas. Sci. Technol. **26**, 012002 (2015).
2. M. Linne, "Imaging in the optically dense regions of a spray: a review of developing techniques," Prog. Energy Combust. Sci. **39**, 403–440 (2013).
3. L. Wang, P. P. Ho, C. Liu, G. Zhang, and R. R. Alfano, "Ballistic 2-d imaging through scattering walls using an ultrafast optical kerr gate," Science **253**, 769–771 (1991).
4. L. Wang, P. P. Ho, X. Liang, H. Dai, and R. R. Alfano, "Kerr-fourier imaging of hidden objects in thick turbid media," Opt. Lett. **18**, 241–243 (1993).
5. L. Wang, P. P. Ho, and R. R. Alfano, "Time-resolved fourier spectrum and imaging in highly scattering media," Appl. Opt. **32**, 5043–5048 (1993).
6. E. Berrocal, D. L. Sedarsky, M. E. Paciaroni, I. V. Meglinski, and M. A. Linne, "Laser light scattering in turbid media part I: experimental and simulated results for the spatial intensity distribution," Opt. Express **15**, 10649–10665 (2007).
7. E. Berrocal, D. L. Sedarsky, M. E. Paciaroni, I. V. Meglinski, and M. A. Linne, "Laser light scattering in turbid media part II: spatial and temporal analysis of individual scattering orders via monte carlo simulation," Opt. Express **17**, 13792–13809 (2009).
8. M. Paciaroni, M. Linne, T. Hall, J. P. Delplanque, and T. Parker, "Single-shot two-dimensional ballistic imaging of the liquid core in an atomizing spray," Atomization Sprays **16**, 51–69 (2006).

#243730 Received 24 Jun 2015; revised 9 Aug 2015; accepted 9 Aug 2015; published 17 Aug 2015

9. J. B. Schmidt, Z. D. Schaefer, T. R. Meyer, S. Roy, S. A. Danczyk, and J. R. Gord, "Ultrafast time-gated ballistic-photon imaging and shadowgraphy in optically dense rocket sprays," Appl. Opt. **48**, B137–B144 (2009).
10. D. Sedarsky, E. Berrocal, and M. Linne, "Quantitative image contrast enhancement in time-gated transillumination of scattering media," Opt. Express **19**, 1866–1883 (2011).
11. D. Barnhart, "Optica software," (www.opticasoftware.com).
12. M. Paciaroni and M. Linne, "Single-shot, two-dimensional ballistic imaging through scattering media," Appl. Opt. **43**, 5100–5109 (2004).
13. E. Hecht, *Optics*, 4th ed. (Addison Wesley Longman Inc., 1998).
14. D. Sedarsky, "Ballistic imaging of transient phenomena in turbid media" (Ph.D. Thesis, Department of Physics, Lund University, 2009).
15. T. Parker and J. Labs, "Diesel fuel spray droplet sizes and volume fractions from the region 25 mm below the orifice," Atomization Sprays **13**, 18 (2003).
16. A. Campillo, S. Shapiro, and B. Suydam, "Relationship of self-focusing to spatial instability modes," Appl. Phys. Lett. **24**, 178–180 (1974)
17. G. Lawrence, "GLAD theory manual, ver. 5.5," (2009). Applied optics research. See www.aor.com.
18. S. Spuler and M. Linne, "Numerical analysis of beam propagation in pulsed cavity ring-down spectroscopy," Appl. Opt. **41**, 2858–2868 (2002).
19. M. Linne, "Analysis of x-ray phase contrast imaging in atomizing sprays," Exp. Fluids **52**, 1201–1218 (2012).
20. M. Linne, "Analysis of x-ray radiography in atomizing sprays," Exp. Fluids **53**, 655–671 (2012).
21. R. A. Ganeev, A. I. Ryasnyansky, N. Ishizawa, M. Baba, M. Suzuki, M. Turu, S. Sakakibara, and H. Kuroda, "Two- and three-photon absorption in CS_2," Opt. Commun. **231**, 431–436 (2004).
22. S. Couris, M. Renard, O. Faucher, B. Lavorel, R. Chaux, E. Koudoumas, and X. Michaut, "An experimental investigation of the nonlinear refractive index (n_2) of carbon disulfide and toluene by spectral shearing interferometry and z-scan techniques," Chem. Phys. Lett. **369**, 318–324 (2003).
23. E. Reynoso Lara, Z. Navarrete Meza, M. D. Iturbe Castillo, C. G. Trevino Palacios, E. Marti Panameno, and M. L. Arroyo Carrasco, "Influence of the photoinduced focal length of a thin nonlinear material in the z-scan technique," Opt. Express **15**, 2517–2529 (2007).
24. H. Kogelnik and T. Li, "Laser beams and resonators," Appl. Opt. **5**, 1550–1567 (1966).
25. A. Samoc, "Dispersion of refractive properties of solvents: chloroform, toluene, benzene, and carbon disulfide in ultraviolet, visible, and near-infrared," J. Appl. Phys. **94**, 6167–6174 (2003).
26. R. A. Ganeev, A. I. Ryasnyansky, M. Baba, M. Suzuki, N. Ishizawa, M. Turu, S. Sakakibara, and H. Kuroda, "Nonlinear refraction in CS_2," Appl. Phys. B **78**, 433–438 (2004).
27. S. Idlahcen, C. Roze, L. Mees, T. Girasole, and J. B. Blaisot, "Sub-picosecond ballistic imaging of a liquid jet," Exp. Fluids **52**, 289–298 (2012).
28. H. Purwar, S. Idlahcen, C. Roze, D. Sedarsky, and J. B. Blaisot, "Collinear, two-color optical kerr effect shutter for ultrafast time-resolved imaging," Opt. Express **22**, 15778–15790 (2014).

1. Introduction

Fuel sprays and the conversion of liquid fuel to combustible fuel vapor are critical factors in the performance of several types of combustion engines. Unfortunately, spray break-up and mixing processes are not well understood; the current state of understanding of primary spray breakup processes is limited. In order to address this problem several new experimental techniques have appeared, providing quantitative information on break-up in the dense spray formation region [1, 2]. Ballistic Imaging (BI) is one such technique.

BI is a line-of-sight optical imaging technique providing high-resolution images of structures hidden within turbid media. This diagnostic is most commonly implemented using commercially available short pulse (*e.g.* $\sim$ 100 fs pulsewidth) lasers and low light level imaging systems. Ballistic imaging was originally developed for imaging through human tissue, and the time-gated approach was reported by the group of Alfano at the City University of New York (see *e.g.* [3–5]). Time-gated ballistic imaging (TGBI) for spray studies has recently been reviewed in detail [2]; therefore, these introductory comments will simply provide context for the current work.

Ballistic imaging passes a laser beam through the spray utilizing specialized optics to filter the light exiting the spray, to extract a high-resolution image of larger liquid structures. BI takes advantage of the very small amount of light passing directly through a dense spray without scattering off-axis from the droplets. Light that passes straight through the droplet cloud surround-

#243730 Received 24 Jun 2015; revised 9 Aug 2015; accepted 9 Aug 2015; published 17 Aug 2015

ing the spray formation region, without droplet interactions, is termed ballistic light. This light exits the spray with unchanged coherence, directional and polarization properties compared to the input beam. Ballistic photons travel the shortest path and exit the spray first. Unfortunately, there are generally not enough ballistic photons to produce single-shot, time-resolved images in a dense spray [2]. The scattering phase functions of the typical droplets sizes (5-20 μm) in sprays have a very strong forward scattering lobe, however, and the bulk of these forward scattered photons are quasi-ballistic; exiting on or very near the centerline and they exit just after the ballistic photons [6, 7]. The combined ballistic and quasi-ballistic light (together called "useful imaging light") is refracted by the larger liquid structures inside the spray. Thus useful imaging light can be used to construct shadow images of larger fluid structures by suppressing the off-axis scattered light from drops that can corrupt more traditional forms of shadowgraphy. BI thus aims to reject almost all of the light headed towards the camera because it is corrupted by multiple scattering off-axis; it preserves only the useful imaging light.

In the current implementation, BI segregates the small amount of useful imaging light by filtering the light signal based on the following characteristic signatures. First, the useful imaging light is nearly co-linear with the input laser beam (soft spatial filtering is used). Second, it retains the polarization of the input beam (polarization filtering). Finally, the useful imaging light is first to exit because it travels the shortest path (time-gating). Time gated ballistic imaging commonly rejects the contribution of multiply scattered off-axis photons with a very fast optical Kerr effect (OKE) time-gate (a very fast external shutter). This allows transmission of useful imaging light while rejecting later arriving photons. The design of the OKE-gate also includes inherent spatial and polarization filtering. This contributes to further filtering of corrupted image light to produce a single-shot ballistic image.

Examples of two OKE-gated optical systems are shown in Figs. 1(a) –1(b). The main difference between the two setups is in the method of relaying the image to the camera. The setup in Fig. 1(a), here called the 4f setup, is similar to the arrangement used in earlier work by Alfano *et al.* [4] which was adapted and used in early BI spray studies [8]. The setup in Fig. 1(b), here called the 2f setup, was first described by Schmidt *et al.* [9] and is less complex. It generated what appeared to be similar image quality compared to the 4f setup. The double lens setup is referred to as 4f since it in principle is a standard 4f correlator used in Fourier optics. The single lens setup, on the other hand, is referred to as 2f since it is a more classical imaging setup and resembles the one-to-one magnification achieved when placing the collecting lens 2f behind the object. The results from Schmidt *et al.* indicated that for time-gated ballistic imaging in atomizing sprays the Fourier-imaging style used in the 4f is not the only option; simpler setups can be used for spray studies. In 2011 Sedarsky *et al.* published a detailed model comparing the 2f imaging setup to a 4f projection system [10]. Here, the 4f system was modeled as a non-focused system as opposed to the experimentally focused one. In the work of Sedarsky *et al.*, the output of a Monte Carlo code which modeled the light scattering in the turbid media was coupled with a commercial ray-tracing code used to model the optical system [11]. The modeling by Sedarsky *et al.*, which produced very good agreement with the experimental contrast transfer functions (CTF) by Paciaroni [12], demonstrated that the size of the scattering particles (*i.e.* their scattering phase function) determines the regimes in which each optical system performs best. In their comparison, contrast from a single spatial frequency (1 line pair/millimeter (lp/mm)) was investigated and the 2f system generated higher contrast than the non-focused 4f in the large-particle limit (15 μm polystyrene spheres (PS) in water). In the small-particle limit (0.7 μm PS spheres in water), on the other hand, the 2f system generated lower contrast. Sedarsky *et al.* argued that the reason for these results lies in the scattering phase function of the spheres. The 2f with its longer object-to-lens distance performs better in situations dominated by forward scattering than in the more diffuse scattering generated by small particles. The op-

#243730 Received 24 Jun 2015; revised 9 Aug 2015; accepted 9 Aug 2015; published 17 Aug 2015

posite can be said about the non-focused 4*f* projection system which preferentially transmits forward scattered light while suppressing diffusively scattered light and, hence, performs better in the small-particle limit. However, the resultant CTFs of the two modeled setups have not been investigated experimentally, neither has a comparison between a focused 4*f* setup and the 2*f* setup.

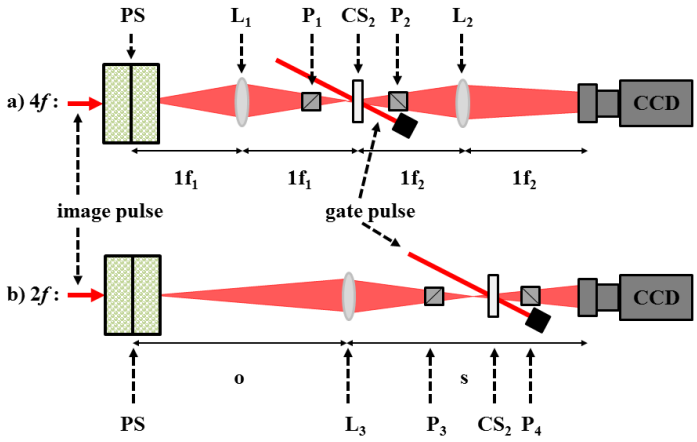

Fig. 1. Optical setups. Part a) shows the 4*f* setup and part b) the 2*f* setup. For USI the polarizers and the CS_2 cell (Kerr medium) were removed and the gate beam blocked.

In the wider ballistic imaging community, the OKE-gate is not always considered a necessity. Many techniques used to segregate high quality image light from corrupted light has been called 'ballistic imaging' in the biomedical literature. In our work, we have noticed that certain sprays with lower optical depths (OD) do not require the OKE-gate in order to generate images of large interior structures with reasonable resolution. In addition to the study of 4*f* and 2*f* setups, therefore, we have conducted a short study to evaluate the contribution of the OKE gate even at lower values of OD.

In this work, we compare the 4*f* and 2*f* TGBI setups. First they were compared experimentally under controlled scattering conditions. To increase understanding of the imaging differences between the two setups caused by aberrations, a series of experiments combined with computational modeling were conducted. Finally, the 2*f* TGBI setup was compared to its non-time-gated equivalent, under the same scattering conditions, to determine when and how the time-gate enhances imaging performance. It should be noted that the non-time-gated shadow imaging technique applied in this work uses the same short laser pulses as used in TGBI, as opposed to broad-band white light shadow images. Throughout this article, this technique will be referred to as ultrafast shadow imaging (USI).

2. Experimental methods

Two different types of experiments were carried out in the 4*f*-2*f* TGBI studies. First, the performance of the two optical systems was evaluated under varying scattering environments. Many of the results indicated that system-based aberrations were generated; therefore, a second style of experiment was focused on aberrations. For the aberration work, the scatterers were removed to make the outcomes more straightforward. All images were flatfield corrected with camera dark current and gate beam scattering subtracted.

The performance of the two imaging setups was quantified using contrast transfer functions. The CTF is related to the system optical transfer function [13], and serves as a metric for the

#243730 Received 24 Jun 2015; revised 9 Aug 2015; accepted 9 Aug 2015; published 17 Aug 2015

dynamic range and spatial resolution of the system [14]. A resolution test chart was imaged both through a series of scattering conditions designed to replicate those of typical diesel fuel sprays issuing into room-temperature air and through a series of non-scattering conditions to identify sources of aberrations. The contrast was measured for a range of single spatial frequencies (line patterns) and from these measurements the CTFs were constructed. Here the contrast for a specific spatial frequency was calculated according to $C = (I_{\max} - I_{\min})/(I_{\max} + I_{\min})$.

For experiments under scattering conditions, the scattering environment was simulated using monodisperse suspensions of polystyrene spheres (PS) mixed with distilled water in varying sizes and concentrations. The test chart (a USAF 1951 resolution test chart) was placed in the center of the scattering medium. The optical system collection angles were matched to compare setups with similar numerical aperture, *i.e.* setups with nominally similar resolution. Ten images under each condition were taken, and CTF mean and standard deviations were calculated.

Fuel spray droplets are formed in a distribution of sizes which roughly fall in the range of 5-20 μm [15]. Thus, 5 μm, 10 μm, 15 μm, and 20 μm fuel droplets in varying concentrations were investigated. Corresponding PS sphere sizes were determined by calculating the Mie scattering phase function for the diesel droplets surrounded by air using a light wavelength of 800 nm. The phase functions were then compared to those of the available PS spheres suspended in water and a nearest match was determined by choosing the sphere sizes yielding the smallest root-mean-square difference. This resulted in the following selection of PS sphere sizes: 3.5 μm, 8.0 μm, 9.7 μm, and 14.9 μm. Here, the standard deviation of the diameter in the different PS suspensions was around 0.1%. In Figs. 2(a) –2(d) the scattering phase functions of the fuel drops together with the phase functions of the corresponding PS spheres can be seen.

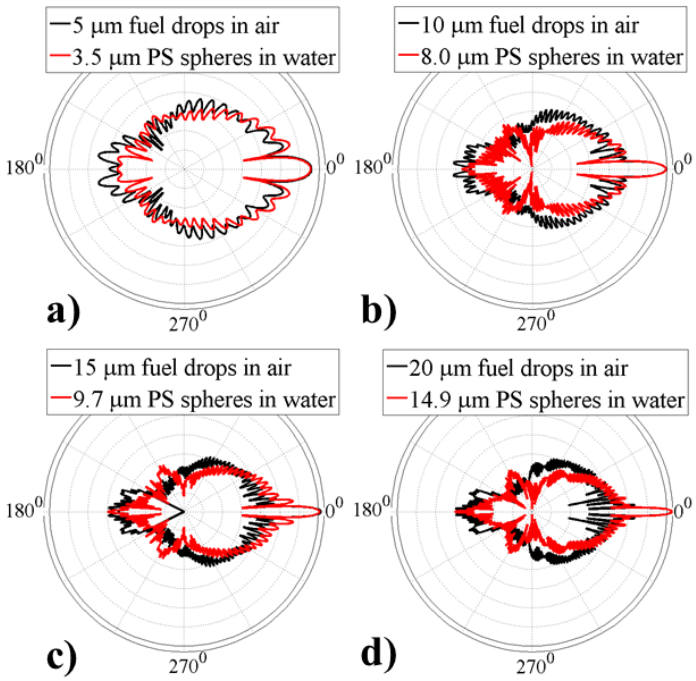

Fig. 2. a) – d) Logarithmic polar plots of the scattering phase functions for 5 μm, 10 μm, 15 μm, and 20 μm fuel drops in air with the corresponding phase functions for the PS spheres in water. 0° corresponds to strictly forward scattering.

Optical Depth (OD) was used to quantify sphere concentrations. OD is formally defined by

#243730 Received 24 Jun 2015; revised 9 Aug 2015; accepted 9 Aug 2015; published 17 Aug 2015

the Beer-Lambert law

$$\frac{I}{I_0} = e^{-\mathrm{OD}},\ OD = n\sigma_{ext}L. \tag{1}$$

Here n, σ_{ext} and L are the number density of spheres, total extinction cross-section, and path length through the scattering medium, respectively. Under the assumption of no absorption, the total extinction cross section can be replaced by the scattering cross-section (σ_{scatt}). $n\sigma_{scatt}$ represents the average number of scattering events taking place on a unit path length. As argued by Linne [2], experimentally measured values for transmission through a spray are a function of the scattering phase function of the particles and the collection angle of the experimental instrument. This complicates discussion of the measured OD for particular sprays or PS suspensions. For this reason, in the work reported here we equate the number of scattering events to the OD. This is justified by the fact that scattering events and OD are roughly similar for this particle size range [7]. Using the scattering cross-sections in Table 1, the relation between OD and number density can be calculated using Eq. (1).

Table 1. Scattering cross-sections for the used PS sphere sizes in water using 800 nm light.

Sphere size	σ_{scatt}
3.5 μm	1.7×10^{-5} mm^2
8.0 μm	1.2×10^{-4} mm^2
9.7 μm	1.4×10^{-4} mm^2
14.9 μm	4.0×10^{-4} mm^2

TGBI aberrations were investigated with a Siemens star chart, with spatial frequencies ranging from 5.7 lp/mm to 115 lp/mm, placed in the cell filled with distilled water. The same collection lens was used for both the $4f$ and $2f$ setups in order to match focal spot sizes and relative positions of the Kerr medium when isolating aberrations. Nine images under each condition were captured and a mean contrast for each condition was obtained from the CTFs. Data variation was calculated from contrast variance for each measured spatial frequency. Variances were subsequently summed and standard deviations calculated. Finally, the $2f$ system was used to compare TGBI and USI under similar conditions.

3. Experimental setups

The experimental configurations are shown in Figs. 1(a) –1(b). Here, the symbols represent the following; PS - a 10 mm path length optical cell for the scattering and non-scattering media with the test chart in the center, L_1-L_3 - achromatic lenses, P_1-P_4 - 15x15 mm^2 clear aperture Glan-Laser polarizers, CS_2 - a 40 mm clear aperture optical cell with 10 mm path length and filled with CS_2 (the Kerr medium), f_1-f_2 are the focal lengths for respective lens, and o and s are the object-to-lens and lens-to-image distances respectively. For the experiments in scattering environments, the following lenses where used: $L_1 = 3$ inch diameter with $f_1 = 250$ mm, $L_2 = 3$ inch diameter with $f_2 = 500$ mm, and $L_3 = 2$ inch diameter with $f_3 = 150$ mm. In the aberration experiments the $4f$ configuration used the same lenses used previously, but the $2f$ used a 3 inch diameter, $f = 250$ mm lens. Minimization of gate beam scattering onto the image plane was achieved through the use of a CS_2 cell with large enough clear aperture to mitigate cell wall scattering through the last OKE-gate polarizer.

In the $4f$ setup (Fig. 1(a)), the object plane is relayed through the Fourier plane and back to the image plane on the screen. The first lens (L_1) is placed a focal length, f_1, from the object plane, and the second lens (L_2) is placed an additional focal length, f_2, behind the Fourier

#243730 Received 24 Jun 2015; revised 9 Aug 2015; accepted 9 Aug 2015; published 17 Aug 2015

plane, or focus, of L_1. A real image displayed a focal length behind L_2 has a magnification, M, given by $M = f_2/f_1$. In TGBI, the OKE-gate is placed between the two lenses. Here the CS_2 cell is placed far enough away from the image beam focal plane for nonlinear distortion effects not to be noticed. Using the published data for the lenses, this setup resulted in an image magnification of two and a collection half angle of 8.7°.

The 2*f* system (Fig. 1(b)) uses a single lens to generate a real image of the object at the screen. A magnified, real image requires an object-to-lens distance of between 1 and 2 focal lengths. Matching the magnification and collection angle of the 4*f* configuration in the PS sphere experiments required the lens to be placed 225 mm behind the test chart. This resulted in an image magnification of two and a collection half angle of 6.4° degrees. In this scheme, the OKE-gate was placed between the lens and the camera. As before, the CS_2 cell was placed away from the focal plane to avoid unwanted nonlinear effects. In the aberration experiments the 2*f* used the same collecting lens as the 4*f*. In this set of experiments both setups had a magnification of two, and for the 2*f* setup the corresponding object-to-lens distance was 375 mm.

A 1 kHz repetition rate chirped-pulse regenerative amplifier (Spectra-Physics Spitfire) providing 4 W of average optical power was used to generate source light for the experiments. It provided pulse widths around 180 fs (Full Width at Half Maximum (FWHM)) centered at 800 nm with a 10 nm (FWHM) bandwidth and a beam diameter of about 8 mm ($1/e^2$). The beam was split into an imaging beam and a gating beam. After the beam splitter, the gating beam was directed through a polarizer/waveplate combination and a retroreflecting time delay (TD) to control polarization, power and timing in relation to the image pulse. In the TGBI configuration, the gating beam was used to induce birefringence in the CS_2, creating an optical shutter time of around 1.5 ps FWHM. In the scattering experiments the gate beam used a pulse energy around 0.7 mJ. In the aberration experiments, on the other hand, the gate pulse energy was varied to investigate distortion effects. After the beam splitter the image beam was passed through a polarizer/wave plate combination providing polarization and power control. The resolution test chart embedded in the center of a cell containing either the PS sphere suspension or pure water, was placed after this first polarizer. In the scattering experiments, the image pulse energy was adjusted to achieve a suitable signal strength depending on the particular scattering condition, while in the aberration experiments it was varied to observe effects of changes to it. The image, for all configurations, was captured with an Andor iXon 885 EMCCD camera. In the USI configurations, the gating beam was blocked and the OKE-gate removed.

4. 4f setup compared with the 2f setup

4.1. TGBI experiments in scattering conditions

In Fig. 3 representative unprocessed raw images of the test chart generated by the TGBI setups can be seen. In the figure, images generated by the 4*f* and the 2*f* setups with 3.5 μm spheres at OD7, and 14.9μm spheres at OD10 are shown. The experimental TGBI results are shown in Figs. 4 and 5 as CTF plots. Based on the standard deviation in the data, a practically useful lower limit for a detectable contrast is ~ 0.15 (based on a 95% confidence interval). In the OD0 case, which was achieved using pure distilled water, the 4*f* and 2*f* setups exhibited ultimate resolutions of roughly 30 lp/mm and 50 lp/mm respectively. The 2*f* setup had notably better image resolution before the introduction of scatterers. With the introduction of scatterers, however, the highest resolvable spatial frequency is similar for both setups for all ODs and sphere sizes. This is an indication that certain finer features in the imaging setups are lost in the presence of scatterers, and scattering controls the ultimate resolution. One reason the two systems differ when there are no scatterers is that the OKE-gate affects the imaging performance of the two systems differently. Finer details are lost due to harder spatial filtering in the 4*f* setup. The

#243730 Received 24 Jun 2015; revised 9 Aug 2015; accepted 9 Aug 2015; published 17 Aug 2015

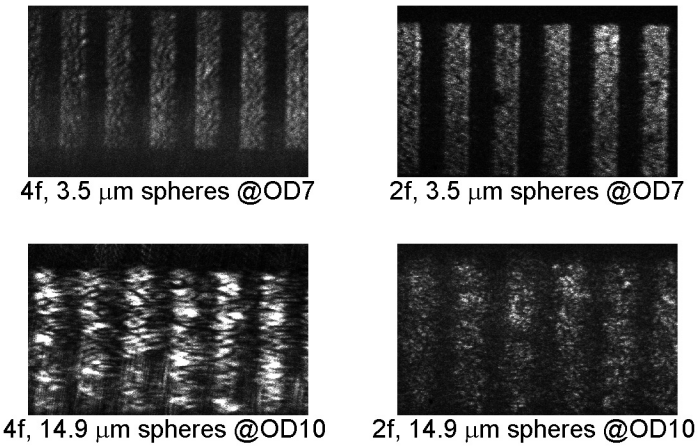

Fig. 3. Representative raw images of a 3.56 lp/mm line pattern for TGBI with 3.5 μm spheres at OD7, and 14.9μm spheres at OD10.

high frequency components visible in the 2f setup, on the other hand, are still present even with scatterers. However, due to the presence of noise introduced by scattered light, the background noise level is higher than the intensity of the high frequency components. Contrast is lost.

To continue the discussion on scattering results, the 2f setup generates higher contrast in the lower sphere size range and in the densest cases. Using larger sphere sizes at moderate ODs, the results are mixed. During the experiments, it was noted that the 4f setup was consistently more sensitive to alignment issues and to changes in the OKE-gate setup. This observation is evidenced in the oscillations of the CTFs, which indicate aberrations in the optical system. Here, one sees that they are present for both setups but more pronounced in the 4f case. The outlying CTFs are the ones from the 3.5 μm spheres at OD10. Here both the 4f and the 2f setups show increasing contrast with increasing spatial frequency up to around 10 lp/mm where the CTF starts to decay.

4.2. TGBI aberration experiments in non-scattering conditions

By examining the CTFs in Figs. 4 and 5, one can see that system aberrations play a noticeable role in image generation by TGBI. Their presence can be both inherent to the TGBI design or caused by optical misalignments. One speculation was that the OKE-gate could be a significant contributor to the aberrations. To further investigate the potential role of the OKE time-gate in the generation of aberrations, two sets of experiments were performed. The first set investigated the influence of image pulse energy coupled with position of the CS_2 cell along the image beam optical axis. The second set investigated the influence of the gate pulse energy. In both experiments, the imaging performance was quantified in terms of CTF, using a Siemens star chart placed in distilled water (a non-scattering environment). The observed changes in mean contrast was for both set of experiments statistically significant based on the Student's t-test, with p-values well below 0.0001.

To investigate the effects of image pulse energy and the position of the CS_2 cell, the gate beam was blocked and the second OKE-gate polarizer rotated to allow transmission. The CS_2 cell was translated along the optical axis as shown in Figs. 1(a) –1(b). Limited by the polarizers, the cell was moved between 10 cm and 45 cm behind the collecting lens (in both setups the image beam had a focal plane $\sim$25 cm behind the collecting lens). Image pulse energies of 10, 25, and 50 μJ were tested. Representative images generated with the 2f setup using 50 μJ image

#243730 Received 24 Jun 2015; revised 9 Aug 2015; accepted 9 Aug 2015; published 17 Aug 2015

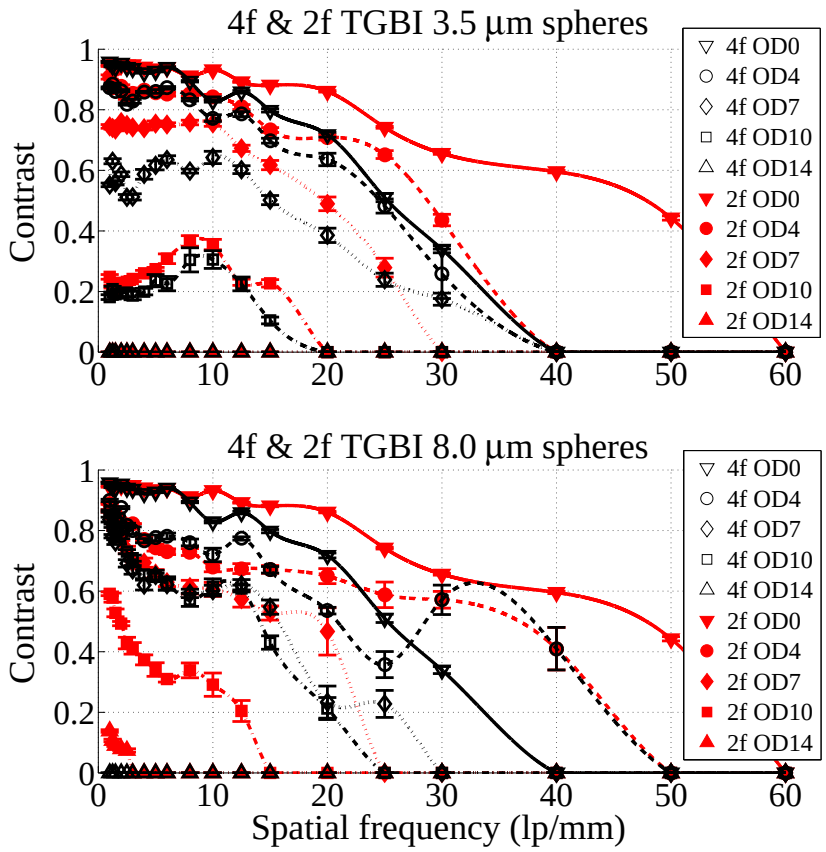

Fig. 4. Experimentally measured CTFs for 4*f* and 2*f* TGBI setups with sphere sizes of 3.5 μm and 8.0 μm. The error bars represent one standard deviation.

pulse energy and with the CS_2 cell placed 26 cm and 38 cm behind the collecting lens are shown in Fig. 6. Here, the effect of placing the CS_2 cell near the focal plane can be seen. The image at 26 cm is significantly distorted compared to the image at 38 cm. The distortion is caused by the higher intensity of the focused image beam. With sufficiently high light intensities, undesirable nonlinear effects in the CS_2 (*e.g.* self-focusing) are generated, which can distort the image information carried in the pulse [16]. The results of moving the CS_2 cell through the image beam focal plane in the 4*f* setup can be seen in Fig. 7. Only the 4*f* results are presented because the 2*f* setup exhibited the same trends. To ease interpretation of the data, and since finer details of the transfer functions are not needed to interpret the results, the mean contrast from between 6.1 - 32.0 lp/mm in each CTF was calculated. The spatial frequency range in the average was chosen to avoid the significantly distorted image center, since calculating contrast there does not provide useful information. Even with this restriction, a clear dependence on position can be observed. All three energy levels produce distortion, manifested by a decrease in mean contrast, with the CS_2 cell close to the focal plane.

In the second set of aberration experiments, effects of varying the gate pulse energy were investigated. Here, the gate beams in Figs. 1(a) –1(b) were unblocked and the OKE-gate polarizers were set with perpendicular transmission axes, *i.e.* the setups were in TGBI mode. For

#243730 Received 24 Jun 2015; revised 9 Aug 2015; accepted 9 Aug 2015; published 17 Aug 2015

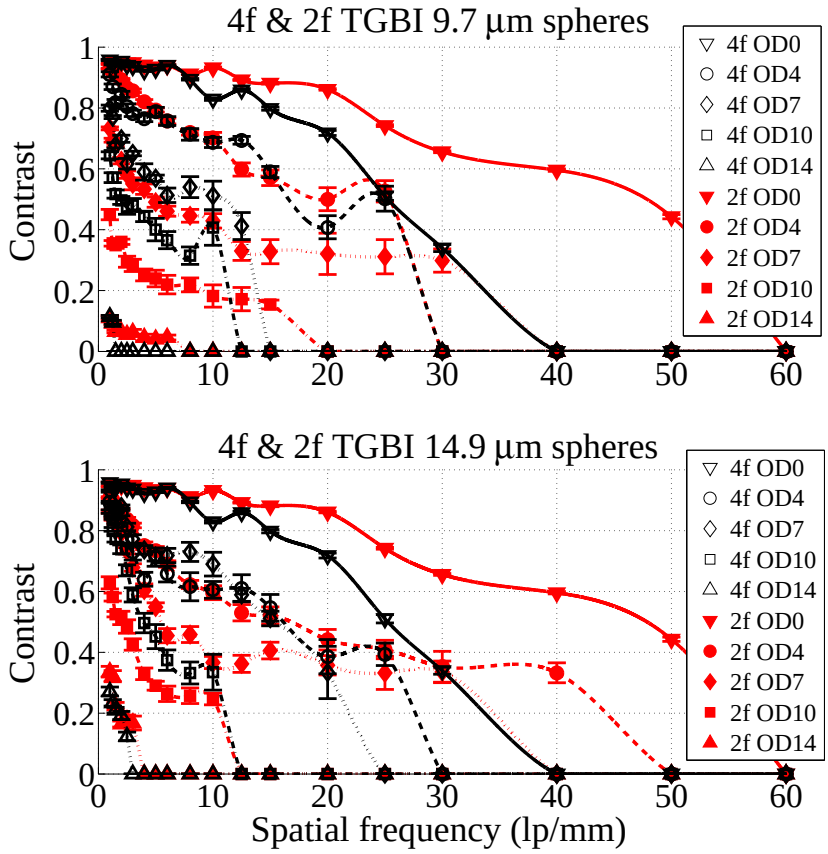

Fig. 5. Experimentally measured CTFs for 4*f* and 2*f* TGBI setups with sphere sizes of 9.7 μm and 14.9 μm. The error bars represent one standard deviation.

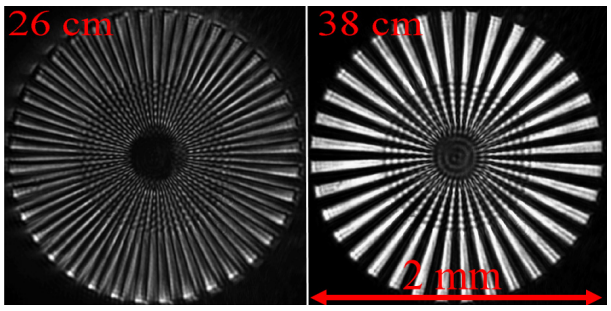

Fig. 6. Comparison of images of the Siemens star target generated with the 2*f* setup using an image pulse energy of 50 μJ with the CS_2 cell placed at 26 cm and 38 cm behind the collecting lens.

#243730 Received 24 Jun 2015; revised 9 Aug 2015; accepted 9 Aug 2015; published 17 Aug 2015

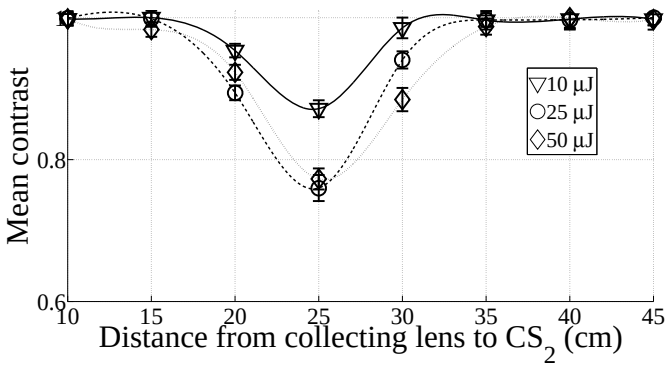

Fig. 7. Mean contrast (average over 6.1-32.0 lp/mm in the CTF) as function of distance between collecting lens and CS_2 cell with the gate beam blocked and the OKE-gate opened for the 4*f* setup. The normalized curves show significant degradation in mean contrast near the focal plane. The error bars represent one standard deviation.

both the 4*f* and 2*f* setups, the CS_2 cell was placed 50 cm behind the collecting lens, and the angle between the image and gate beams was $\sim 11^\circ$. The experiment was performed by first aligning and optimizing the image quality at maximum gate pulse energy for each setup. This corresponded to 0.66 mJ and 0.68 mJ gate pulse energies for the 4*f* and 2*f* respectively. The gate pulse energy was subsequently decreased in steps. The results can be seen in Fig. 8, presented again as the mean contrast over 6.1 - 32.0 lp/mm. In this set of experiments, a significant differ-

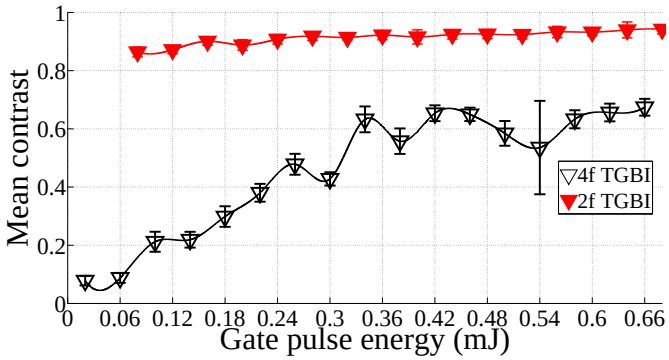

Fig. 8. Mean contrast (average over 6.1-32.0 lp/mm in the CTF) as function of gate pulse energy for 4*f* and 2*f* setups. The error bars represent one standard deviation.

ence between the two setups can be detected. The mean contrast of the 2*f* setup decreases only marginally when the gate pulse energy is decreased. The 4*f* setup, on the other hand, exhibits a significant reduction in mean contrast.

4.3. Computational modeling of the optical setups

The TGBI experiments indicate that there are differences between the two setups regarding how alignment and aberrations affect the images that are produced. To gain a better understanding, the two setups were modeled in GLAD which is a commercial physical optics code [17] that

#243730 Received 24 Jun 2015; revised 9 Aug 2015; accepted 9 Aug 2015; published 17 Aug 2015

has been used in the past to analyze cavity enhanced absorption [18] and x-ray based spray diagnostics [19, 20]. The code and its use are described in more detail in those papers. In short, GLAD solves the full electromagnetic wave propagation for nearly collimated beams. In this work, the response of the optical systems to lens misalignment and then the response to changes in the OKE-gate setup were modeled.

4.3.1. Model definition

Here, the light pulses were modeled as single wavelength beams (*i.e.* no bandwidth or temporal effects were included). The lenses were modeled as three-surface representations for the achromatic doublets used in the non-scattering experiments, and the polarizers were modeled as isotropic media with the correct dimensions and refractive indices. To approximate a point source, a diverging Gaussian beam with a waist radius of 4 μm and a wavelength of 800 nm was placed with the waist in the object plane, and propagated through the system to the image plane. In the image plane, a one-dimensional intensity pattern was recorded. Using this pseudo Point Spread Function (PSF), the CTF could be estimated by Fourier transformation of the PSF. It should be noted that, since an ideal point source was not used, the resulting CTFs cannot be directly compared with experimental data. Setup response and trends due to misalignments and inherent aberrations, however, will be captured within this approximation. The optical setups were aligned by minimizing spot sizes in the image plane while keeping the position of the collecting lens as described in section 3. In the case of the $2f$ setup, this is straightforward. However, in the case of the $4f$ setup, positioning of the last lens included re-collimation of an originally collimated beam emanating from the object plane.

To model image beam propagation through the CS_2, potential sources of aberration must be identified. Experimental observation established that both image and gate pulse energies can affect the CTF. If, however, the CS_2 cell is placed far enough from the image beam focal plane, non-linear effects from a focused beam can be neglected. This is representative of the experiment leading to Fig. 8. In this arrangement, the primary source of aberration is the gate beam.

CS_2has negligible linear absorption around 800 nm, and with pulse repetition rates of 1 kHz effects due to non-linear absorption are insignificant [21, 22]. Thus, thermal lensing effects are not significant. Another potential source of aberration is the OKE induced spatial refractive index change. Due to the intensity profile of the gate beam a change in the refractive index will be induced along its polarization axis. Since there is an angle between the relative polarization states of the image and gate beams (optimally the angle should be 45°), the image beam's two polarization components will experience different refractive indices and a polarization rotation of the image beam will occur. However, due to the intensity profile there will also be differences in the refractive index along the component of the image beam parallel to the polarization axis of the gate beam. This refractive index anisotropy has the potential to induce aberrations in an optical setup. It can be expressed as

$$n(r_g,t) = n_0 + n_2 I_g(r_g,t). \tag{2}$$

Here n is the refractive index profile, r_g the radial coordinate along the polarization axis of the gate beam, n_0 the linear refractive index, n_2 the non-linear refractive index, t time, and I_g the gate beam intensity.

An approximate analytical solution can be obtained by using the parabolic approximation for the gate beam by Lara *et al.* and the Gradient Index (GRIN) lens expressions by Kogelnik & Li [23, 24]. We assume a Gaussian beam profile of the form

$$I_g(r_g,t) = \frac{2P_p}{\pi\omega^2}\exp\left(-\frac{2r_g^2}{\omega^2} - \frac{\ln(2)t^2}{\tau^2}\right), \tag{3}$$

#243730 Received 24 Jun 2015; revised 9 Aug 2015; accepted 9 Aug 2015; published 17 Aug 2015

where $P_p \approx 0.94E_p/\tau$ is the peak power, E_p the total pulse energy, τ the FWHM length of the pulse, and ω the beam radius ($1/e^2$). Following the derivation by Lara *et al.* and taking the temporal dependence into account only through the magnitude of the peak power, the Gaussian shaped refractive index can be approximated as a parabolic function:

$$n(r_g) \approx n_0 + \frac{2n_2P_p}{\pi\omega^2} - \frac{4n_2P_p}{\pi\omega^4}r_g^2. \tag{4}$$

It can be shown that the induced refractive index anisotropy will act as a GRIN lens with a focal length given by

$$f_{\text{GRIN}} = \frac{1}{n_0'\gamma\sin(\gamma L)}. \tag{5}$$

Here $n_0' = n_0 + 2n_2P_p/(\pi\omega^2)$, $n_2' = 8n_2P_p/(\pi\omega^4)$, $\gamma = \sqrt{n_2'/n_0'}$, and L the path length inside the Kerr medium. Samoc has reported linear refractive index values of 1.6056 and Ganeev *et al.* reported a nonlinear index of $3\cdot10^{-19}$ m^2/W [25,26] for CS_2. Using these values together with a gate pulse energy of 0.7 mJ, a 100 fs pulse length, a 4 mm beam radius, and a CS_2 path length of 1 cm, the corresponding focal length can be calculated. We find that the induced refractive index anisotropy will have a focusing effect with a focal length around 5 m. This effect will act in a crossed-beam geometry and only be active along the polarization axis of the gate beam. Consequently, within this parabolic approximation in the crossed beam geometry, the image beam will experience a skewed cylindrical GRIN lens with a focusing power depending on the peak power of the gate pulse. Since this lensing effect is due to the nonlinear refractive index of the medium it is not restricted to CS_2, it will appear in solid-state Kerr media as well. This source of aberration was implemented in the models of the two TGBI setups. For simplicity, however, the cylinder-lens nature of the GRIN lens is ignored in the models; this effect is modeled as a spherical lensing.

In the GLAD model, the lensing effect was approximated as a series of transversely aligned and offset GRIN lenses with thickness Δz and a refractive index n_0. This implies that apart from offsetting the center of aberration for each GRIN slice, cosine effects due to the oblique gate beam angle are ignored. The initial center of the GRIN aberration is given by:

$$X_0 = X_{\text{offset}} + 0.5L\tan(\theta). \tag{6}$$

Here X_{offset} is the offset in the transverse x-direction and θ is the relative angle between the image and gate beams. In each step (j) the center of the GRIN lens (X_{dec}) is calculated according to

$$X_{\text{dec}}(j) = X_0 - \tan(\theta)\sum_1^j \Delta z. \tag{7}$$

Here it is apparent that if there is no offset Eqs. (6) and (7) yields a symmetric GRIN lens around the center of the Kerr medium ($L/2$). In Fig. 9 an illustration of how the GRIN effect was implemented is shown.

In the calculations, the radius of the GRIN lens was chosen to be large enough to cover the image beam, regardless of angle and transverse offset. The step size (Δz) was taken to be 40 μm which implies calculation of 250 steps in the GRIN model to achieve the 1 cm CS2 path length. The results were checked for grid size dependence and a sufficiently small grid was chosen to avoid that problem. In Fig. 10 the focal length of the GRIN model is compared with the analytical expression in Eq. (5). The computational model agrees fairly well with the analytical results. With gate pulse energies of 2 mJ and higher the differences between the focal lengths were less than 8%, but in the limit of low gate pulse energies the computational model tends to predict stronger focusing than the analytical model. Here, with a 0.1 mJ gate pulse the difference in focal lengths predicted by the models was around 25%.

#243730 Received 24 Jun 2015; revised 9 Aug 2015; accepted 9 Aug 2015; published 17 Aug 2015

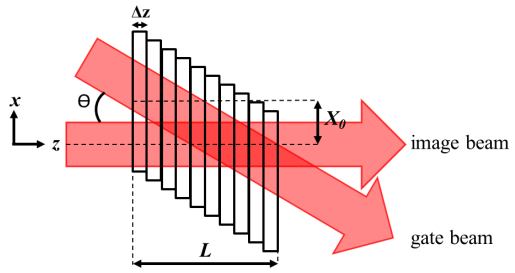

Fig. 9. Illustration of the GRIN effect model.

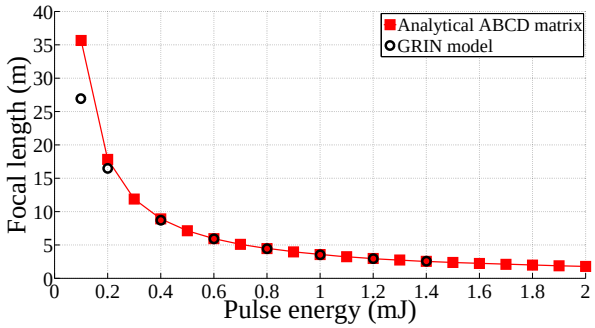

Fig. 10. Comparison of the GRIN model with the analytical ABCD matrix results from Eq. (5). In both cases a pulse length of 100 fs was assumed. In the computational model a 4 mm radius Gaussian beam was propagated through the GRIN model which here was implemented with $\theta = 0$ and no transverse offset.

4.3.2. Modeling results

The model defined in section 4.3.1 was used to observe changes in imaging performance when varying model dependent parameters. To investigate the response to lens misalignments, the collecting lens was displaced along the optical axis, in the transverse direction, and tilted with respect to the optical axis while keeping the other components unchanged from the aligned case. In these cases the GRIN effect of the Kerr medium was not applied (*i.e.* $E_p = 0$). The collecting lens was moved in steps from 0 mm to 0.3 mm along the optic axis, from 0 to 3 mm in the transverse direction, and tilted from 0 to 4 degrees around the optic axis. In Fig. 11 the results of misalignment of the collecting lens along the optic axis are shown. Here, the $4f$-system starts to display oscillations in the CTF with a 0.2 mm increase of the object to collecting lens distance. The magnitude of the oscillations in the $4f$ setup vary with changes in the lens displacement. The $2f$-system, on the other hand, shows smooth variations in contrast while being subject to the misalignments. The results for transverse misalignment of the collecting lens show the same behavior. The $4f$ setup starts to develop oscillations in the CTF with minor misalignments and the $2f$ setup undergoes a smooth decay in the CTF. In the case of tilting the collecting lens relative the optic axis, both systems show the same response and exhibit a smooth decay in the CTF up to 3° where oscillations start to become significant.

In Fig. 12 the results of changing the gate pulse energy (E_p) with the gate beam and image beam arranged in a collinear geometry are shown. In this case, the position of the image plane was optimized for each gate pulse energy value to achieve the best PSF possible. Here, at relatively low gate pulse energies (∼0.3 mJ) the GRIN effect introduces oscillations in the

#243730 Received 24 Jun 2015; revised 9 Aug 2015; accepted 9 Aug 2015; published 17 Aug 2015

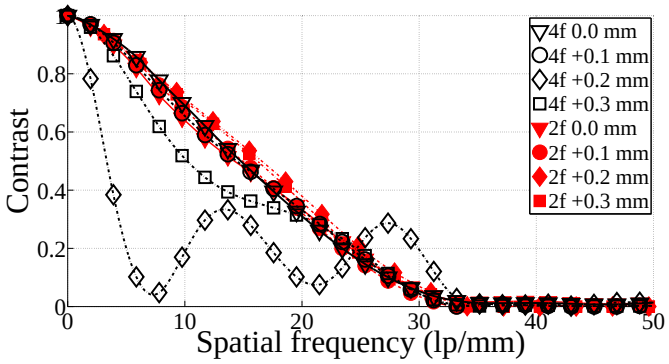

Fig. 11. Model CTFs showing effects of misalignment of the collecting lens along the optic axis in the computational model. The CS_2 is modeled as an isotropic medium ($E_p = 0$).

CTF which cannot be avoided completely by optimizing the image plane position. Both setups were affected by changes in gate pulse energy. If the image plane position was not optimized, the same behavior of the CTFs occurred but at lower gate pulse energies. This result could appear to disagree with Fig. 8. The mean contrast values plotted in Fig. 8 represent an average over a broad spatial frequency range; the same range across which the model and experiments disagree the most. The model is a simplified representation used to evaluate relative sensitivity to changes in various parameters like the gate pulse energy, but the model results cannot be directly compared with experiments. Differences between the model and experiment include re-optimization of the image plane position (done in modeling but not in experiments), the assumption of a steady state in the model OKE gate, and the finite size of the point source used in the model.

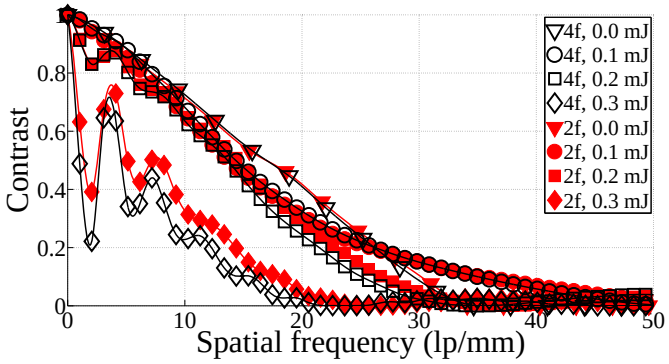

Fig. 12. Model CTFs showing effects of changes in the gate pulse energy (E_p) in the computational model with $\theta = 0$, $\tau = 100$ fs, and $X_{\text{offset}} = 0$.

Figure 13 shows the effect of changing the gate beam angle (θ). Here, the gate pulse energy was 0.2 mJ, the transverse offset 0 mm, and θ was varied between 0° and 30°. The position of the image plane was optimized for the 0.2 mJ gate pulse energy in a collinear geometry. Neither of the setups were significantly affected by the increase in θ, but as can be seen in the magnified part of the graph; there was no effect on the $2f$ setup but the $4f$ setup exhibited a small decrease

#243730 Received 24 Jun 2015; revised 9 Aug 2015; accepted 9 Aug 2015; published 17 Aug 2015

in the CTF with increasing gate beam angle.

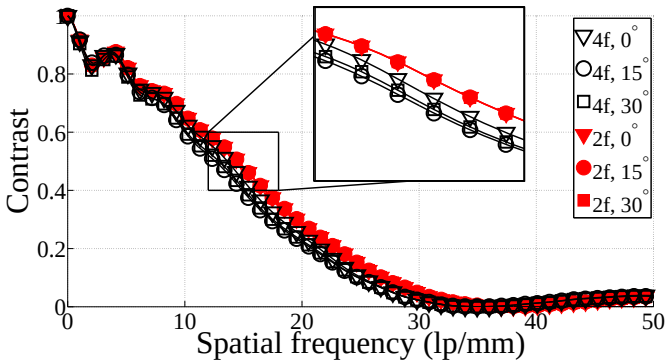

Fig. 13. Model CTFs showing effects of changes in the gate beam angle (θ) in the computational model with $E_p = 0.2$ mJ, $\tau = 100$ fs, and $X_{\text{offset}} = 0$.

In Fig. 14, changes in the CTF caused by variations of the gate beam offset (X_{offset}) can be seen. Here the gate pulse energy was 0.2 mJ, the gate beam angle was 20°, and the transverse offset was varied between 0 mm and 2 mm. In this case the image plane position was optimized for the gate pulse energy in a collinear geometry. A significant effect of increasing the offset can be seen for both setups. The 4*f*, however, was affected more strongly.

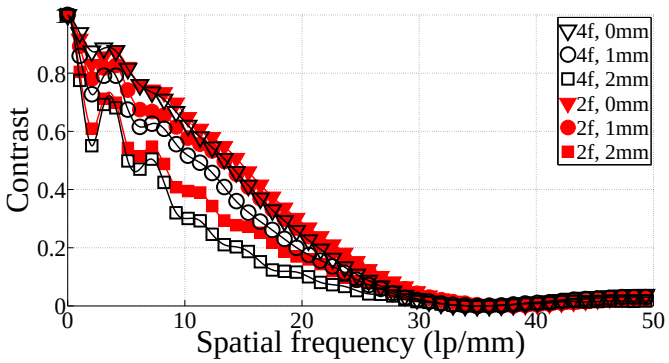

Fig. 14. Model CTFs showing effects of changes in the gate offset (X_{offset}) in the computational model with $E_p = 0.2$ mJ, $\theta = 20°$, $\tau = 100$ fs.

While very careful alignment of the 4*f* system can produce good results, for our cases the 2*f* system is more robust to misalignment and hence and more easily used. For that reason it was used for the study that follows.

5. TGBI compared with USI

In Figs. 15 and 16 the results of the comparison between the TGBI and USI setups are shown. The 2*f* setup was used in this comparison. Also here, the standard deviation in the data indicated a useful lower limit for detectable contrast ~ 0.15 (based on a 95% confidence interval). As expected the ultimate resolution of USI OD0 is superior to the TGBI case owing to softer

#243730 Received 24 Jun 2015; revised 9 Aug 2015; accepted 9 Aug 2015; published 17 Aug 2015

spatial filtering and lack of distortion introduced by the time gate. In this case, with scattering spheres present, TGBI generates higher contrast for most sphere sizes and OD's. Looking at the highest resolvable spatial frequency, one sees the same trend. It is only the 3.53 μm spheres at OD4 and OD7, and 9.7 μm at OD4 that generate higher spatial resolution for USI. A 2f USI data trend shows higher maximum resolvable spatial frequencies and lower overall contrast for the small sphere sizes than for the larger ones. The opposite is true for larger spheres; here, the overall contrast is higher but the ultimate resolution is lower than in the small sphere cases. This behavior can be attributed to differences in the scattering phase function which is more uniform for the smaller spheres while the probability for forward scattering increases with sphere size. The result is that while more uniform scattering introduces almost constant background noise uniformly decreasing contrast, the larger spheres with a dominant forward scattering lobe, hold the contrast to a higher level until angular spreading of the forward lobe interferes with the size of the line pattern. Here, the contrast is significantly reduced.

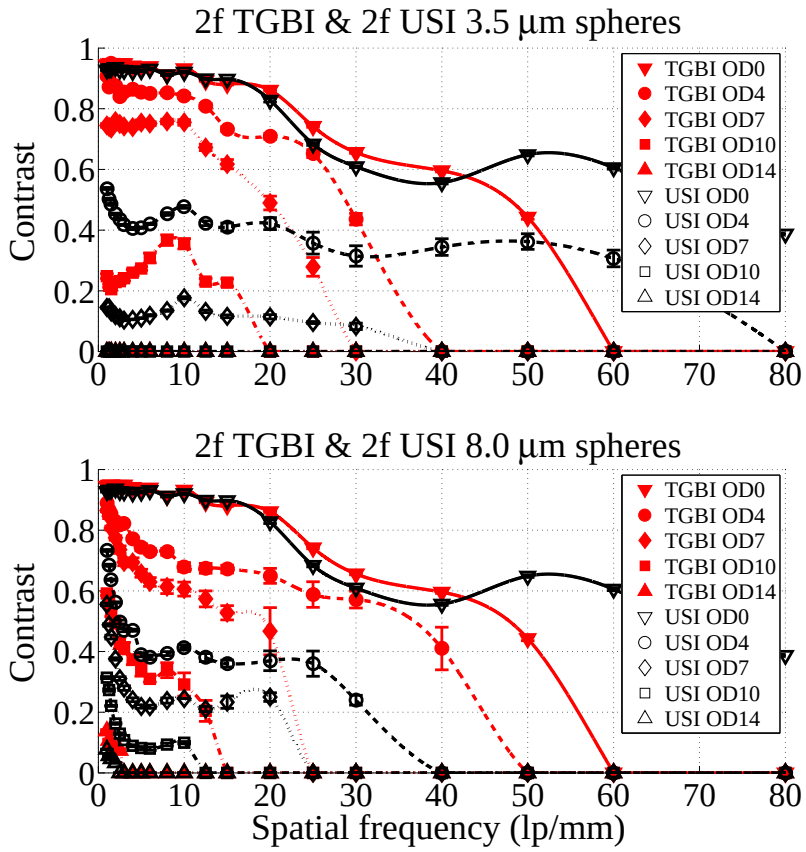

Fig. 15. Experimentally measured CTFs for 2f TGBI and USI setups with sphere sizes of 3.5 μm and 8.0 μm. The error bars represent one standard deviation.

#243730 Received 24 Jun 2015; revised 9 Aug 2015; accepted 9 Aug 2015; published 17 Aug 2015

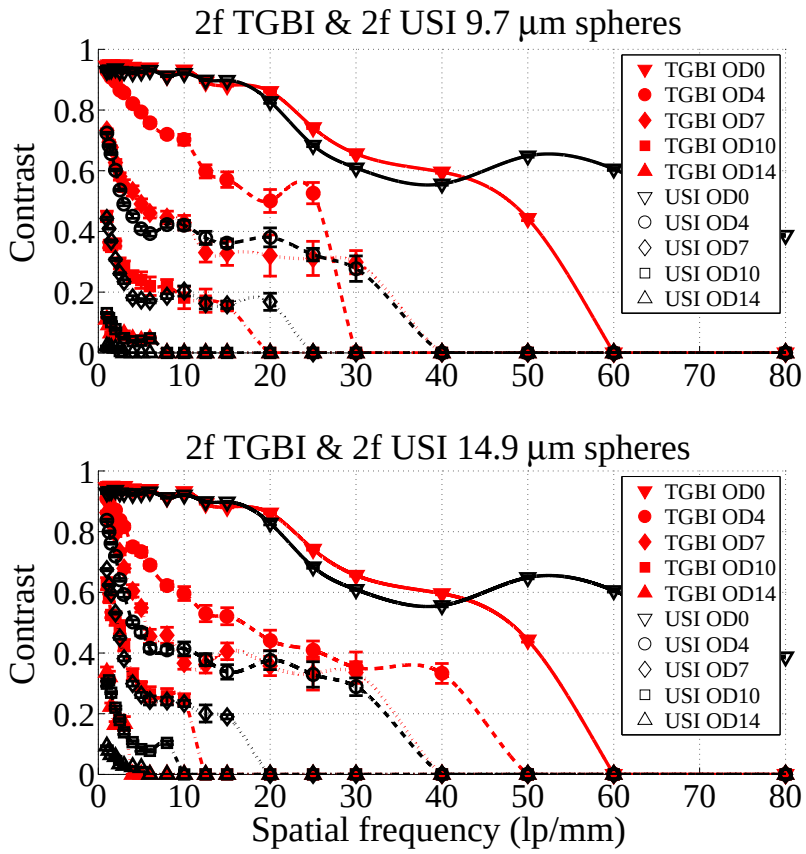

Fig. 16. Experimentally measured CTFs for $2f$ TGBI and USI setups with sphere sizes of 9.7 μm and 14.9 μm. The error bars represent one standard deviation.

6. Conclusion

In this work, we have investigated two different optical setups that have been used in TGBI of sprays in the past. The experimental results showed that, in terms of ultimate resolution, the two setups performed similarly in the presence of scatterers. In terms of contrast, the $2f$ setup performed better in the lower scatterer size range and in the densest cases. With larger scatterer sizes at moderate ODs, the results are mixed. Oscillations in the CTFs, which are indications of system aberrations, are present for both setups but more pronounced in the $4f$ case. The experiments indicated that the $2f$ setup is less sensitive to alignment issues and to variations and fluctuations in the OKE-gate setup.

To gain a better understanding of the sources of aberrations and the difference in sensitivity to them, a set of experiments combined with modeling were performed. It was shown that positioning of the Kerr medium along the optic axis is important since the image beam, when focused, can generate unwanted non-linear lensing effects. It should be noted that the experiments did not investigate spatial filtering effects of the image information due to the finite size of the gate beam. In experiments with an active OKE-gate, there will be a trade-off between mitigating unwanted non-linear effects and minimizing gate beam induced spatial filtering. It was also shown that variations in the gate energy affect the two setups differently. The experi-

#243730 Received 24 Jun 2015; revised 9 Aug 2015; accepted 9 Aug 2015; published 17 Aug 2015

mental results indicate that the 4f setup is more sensitive to variations in the gate pulse energy than the 2f setup.

An analytical investigation indicates that the gate pulse generates a focusing effect in the Kerr medium which induces image distortions. By modeling this lensing effect with a parabolic approximation, it was shown that both setups were affected by changes in the gate beam energy and by induced asymmetries introduced by moving the gate beam in the transverse direction. The 4f setup, however, exhibited a more significant degradation in imaging performance as a result of these factors. Furthermore, it appears that the relative angle between the gate beam and the image beam, or the 'skewedness' of the induced lens, is not significant. However, it should be pointed out that, in the model, the cylinder-lens nature of the induced lensing effect has been ignored. For simplicity, this effect was modelled as a spherical lensing process. Furthermore, spatio-temporal effects on image information transmission have not been considered within this approximation. These effects, however, typically only become significant at sub-picosecond OKE-gates. For further discussion on this issue see for example work published by the group at CORIA [27, 28].

The investigations of the two different optical setups indicate that the 2f system is more robust to misalignment and, hence, more easily used. It is less prone to image distortions caused by component misalignments, changes in object plane position, and variations in the OKE-gate setup.

When comparing the best performing TGBI setup to its USI equivalent, in order to determine cases when the OKE-gate enhances imaging performance, it was shown that the TGBI setup generated higher contrast for most PS sphere sizes and ODs. In terms of resolution it was only in the lower scatterer size range at low ODs that the USI generated higher spatial resolution than the TGBI setup.

Acknowledgments

The authors gratefully acknowledge the Swedish Research Council, the Swedish Energy Agency, and the Knut and Alice Wallenberg Foundation for funding the work.

#243730 Received 24 Jun 2015; revised 9 Aug 2015; accepted 9 Aug 2015; published 17 Aug 2015